Microwave-Assisted Oxidation of Electrospun Turbostratic Carbon Nanofibers for Tailoring Energy Storage Capabilities

Xianwen Mao[a], Xiaoqing Yang[a], Jie Wu[b], Wenda Tian[a], Gregory C. Rutledge*[a] and T. Alan Hatton*[a]

[a]Department of Chemical Engineering, Massachusetts Institute of Technology, 77 Massachusetts Avenue, Cambridge,Massachusetts, 02139, USA
[b]Department of Chemistry, Massachusetts Institute of Technology, 77 Massachusetts Avenue, Cambridge,Massachusetts, 02139, USA
* E-mail: tahatton@mit.edu, rutledge@mit.edu

Abstract: We report the systematic structural manipulation of turbostratic electrospun carbon nanofibers (ECNFs) using a microwave-assisted oxidation process, which is extremely rapid, highly controllable, and affords controlled variation of the capacitive energy storage capabilities of ECNFs. We find a non-monotonic relationship between the oxidation degree of ECNFs and their electrocapacitive performance, and present a detailed study on the electronic and crystalline structures of ECNFs to elucidate the origin of this non-monotonic relation. The ECNFs with an optimized oxidation level show ultrahigh capacitances at high operation rates, exceptional cycling performance and an excellent energy-power combination. We have identified three key factors required for optimal energy storage performance for turbostratic carbon systems: (i) an abundance of surface oxides, (ii) microstructural integrity and (iii) an appropriate interlayer spacing.

1. Introduction

Carbon materials are important for many electrochemical applications due to the wide range of electron-transfer and charge-storage properties that can be achieved.[1-3] Judicious structural manipulation of carbon to vary its chemical, electronic, and crystalline properties is key to the design of many high-performance electrochemical devices such as fuel cells,[4] lithium-ion batteries,[5] and supercapacitors.[6] Oxidation is one of the most important routes to manipulating carbon,[7-9] as the electronic and electrochemical properties of carbon materials (e.g., valence band structure[10, 11] and capacitive performance[12]) depend strongly on the oxidation level of the carbon. Thus controllable carbon oxidation processes with high efficiencies are of great significance.

Electrospun carbon nanofibers (ECNFs) prepared by electrospinning and carbonization have been attracting increasing interest.[13-23] The development of structural modification strategies for ECNFs as well as an understanding of structure-property relationships is desirable to guide the use of these materials. Microwave irradiation, which reduces reaction time dramatically due to the unique microwave dielectric heating mechanism,[24] has enabled efficient preparation and modification of various materials such as metal-organic frameworks,[25] graphene sheets,[26] nanoparticles,[27] and metal oxide/graphene hybrids.[28] However, to the best of our knowledge, microwave-assisted oxidation of ECNFs has not yet been documented, as noted in the comprehensive review of structure modification strategies for ECNFs by Inagaki *et al*.[13] Common methods to control ECNF structures and properties include variation of carbonization conditions[15, 20, 21] and incorporation of functional ingredients such as Pd,[16] Si,[17] Sn,[18] and Pt[29] nanoparticles.

Polyacrylonitrile (PAN)-derived ECNFs[21, 23] are structurally different from CNTs and graphite[7-9] in that they exhibit turbostratic carbon structures with nanosized graphite domains and abundant edge defects. Defect-rich carbon materials (*e.g.*, nanographite,[30, 31] vertically aligned carbon fibers,[32] and heteroatom-doped graphene)[33, 34] are superior to defect-free systems for several important electrochemical applications, such as sensing, electrocatalysis, and energy storage.[1, 2] Therefore it is of great interest to study the controlled oxidation of defect-rich carbon systems and obtain new insights into their microstructural evolution upon oxidation.

Supercapacitors have attracted widespread attention as promising energy storage devices because of their high power capability, long cycle life, low maintenance, and high reliability.[35] Energy storage in supercapacitors can involve two mechanisms: (i) the formation of a layer of ions adsorbed on the oppositely charged electrode surface, which leads to double layer (DL) capacitance, and (ii) surface redox reactions, which give rise to pseudocapacitance. Carbonaceous materials are well-known examples of DL capacitive materials.[2, 35] However, carbon-based electrocapacitive systems usually exhibit moderate specific capacitances, especially at high operation rates; for many carbon systems of various forms,[36-47] the optimal capacitance value obtained at a high scan rate of 0.1 V/s or at a high current density of 1 A/g is typically 50–150 F/g, and rarely exceeds 200 F/g. Nonetheless, carbon electrodes are still the most popular choice to date for use in commercial supercapacitor devices due to their ease of synthesis, low cost, and exceptional chemical and electrochemical stability.[48-50] Metal oxides (e.g., RuO_2,[51, 52] MnO_2[53, 54]) and electroactive polymers (e.g., polyaniline,[55, 56] polyvinylferrocene)[57, 58] exhibit pseudocapacitive characteristics, and have been shown to deliver remarkably higher capacitance values than those of carbon materials possessing only DL capacitances. However, several challenges still remain - the high cost of Ru-based oxides may prohibit them from use in practical applications, while the cycling instability and the poor rate performance of Mn-based oxides and electroactive polymers remain critical issues that require careful examination.[49, 59, 60] Carbon materials functionalized with heteroatom chemical moieties have recently attracted interest for capacitive energy storage. These materials can exhibit high specific capacitances and energy densities due to the heteroatom-induced pseudocapacitance, while simultaneously displaying the merits of carbon electrodes such as

excellent cycling stability and high power densities.[49, 59-62] The key to exceptional electrocapacitive performance is the introduction of ample heteroatom functional groups while simultaneously maintaining good electron/ion transport properties.

Herein we report the systematic structural manipulation of PAN-derived turbostratic ECNFs by a microwave-assisted oxidation process. The microwave-based treatment used here is extremely rapid (completed within a few minutes) and also highly controllable; slight variations of the microwave irradiation time can lead to significant and controllable changes in the defect concentration and oxidation degree of ECNFs. Notably, such changes are unobtainable using conventional heating under the same experimental conditions. Moreover, we demonstrate, for the first time, that this microwave-assisted oxidation process can be used to vary the capacitive energy storage capabilities of ECNFs. Previously, control over the capacitive performance of ECNFs was achieved through use of different polymers as carbon precursors,[63-72] and addition of $ZnCl_2$,[15] V_2O_5,[73] or silver nanoparticles.[74, 75] Interestingly, we find a non-monotonic relationship between the oxidation degree of ECNFs and their electrocapacitive performance. Finally, we present a detailed study on the dependence of the electronic and crystalline structures of ECNFs on the oxidation degree to elucidate the origin of this non-monotonic relation.

Remarkably, the ECNFs with an optimized oxidation degree deliver ultrahigh capacitances at high operation rates (e.g., 345 F/g at 0.1 V/s or 338 F/g at 1 A/g). These values, obtained using two-electrode symmetrical supercapacitor cells with aqueous electrolytes, are higher than the capacitances obtained under the same conditions for all known ECNF supercapacitor systems and many other state-of-the-art carbon-based capacitive materials (see **Supporting Information (SI), Table S1**). This material also exhibits an excellent energy-power combination (the energy density reaches 24.8−46.9 Wh/kg when the power density is maintained at high levels of 10^5−10^4 W/kg), as well as exceptional cycling stability (98% capacitance retention after 10,000 cycles). Additionally, we have identified three key factors required for optimal energy storage performance for turbostratic carbon systems: (i) an abundance of surface oxides, (ii) microstructural integrity and (iii) an appropriate interlayer spacing. This understanding, together with our in-depth examination of the electrochemical, electronic, and crystalline properties of turbostratic ECNFs, may provide valuable insights into structural optimization of other defect-rich graphitic systems[30-34] for a wide range of applications such as (electro)catalysis, electrochemical biosensing, controlled molecular packing, and band structure engineering. [1, 2, 30-34, 76-78]

2. Results and Discussion

2.1. Structural Manipulation of Turbostratic ECNFs Using Microwave-Assisted Oxidation

The microwave-assisted oxidation of as-synthesized ECNFs[21] was performed in a mixture of $KMnO_4/H_2SO_4/H_3PO_4$ using a CEM microwave reactor (Discover S System) at a power of 200 W and a frequency of 2.45 GHz (for details, see **SI Methods**). We studied the structural evolution of ECNFs as a function of microwave irradiation time for times up to 15 min. Hereafter, untreated ECNFs and selected results corresponding to samples microwave-irradiated for 2, 3, and 5 min are denoted as uECNF, ECNF-M2, ECNF-M3, and ECNF-M5, respectively. High-resolution transmission electron microscopy (HR-TEM) images (**Figure 1a**) show that uECNF exhibited smooth surfaces while the treated samples displayed relatively wrinkled surfaces. The corrugation of the fiber surface may be attributed to disruption of sp^2-conjugated structures by introduction of defects upon oxidation. Indeed, Raman spectroscopy measurements show that the R_I value (an indicator of the carbon defect content)[78] increased monotonically for the sequence uECNF, ECNF-M2, ECNF-M3 and ECNF-M5 (**Figure 1b**); these observations suggest that a longer treatment resulted in more defects. The Raman spectra are shown in the **SI Figure S3**. The R_I value is defined as the intensity of the *D*-band at ~1330 cm^{-1} devided by the intensity of the *G*-band at ~1590 cm^{-1}; for calculation details, see **SI Methods**. **Table 1** summarizes the surface characteristics of the unmodified and treated carbon fibers, determined from nitrogen adsorption/desorption measurements at 77 K based on the Brunauer-Emmett-Teller and Barrett-Joiner-Halenda methods. The treated ECNFs had slightly higher specific surface areas (SSAs) and total pore volumes (V_{total}) than did the untreated sample. Also, the microwave-assisted modification process led to an increase in $V_{meso}/(V_{micro}+V_{meso})$, where V_{meso} is the mesopore volume and V_{micro} is the micropore volume. Such enhanced mesoporosity may improve the ion adsorption ability of carbon surfaces and could be beneficial for supercapacitor applications.[15, 69] Wide-range X-ray photoelectron spectra (XPS) (**Figure 1c**) show that the relative intensity of the oxygen peak at 564 eV increased with irradiation time. Quantitatively, the O/C ratio (see **SI Methods** for calculation details) increased from 0.08 ± 0.01 to 0.44 ± 0.02 to 0.56 ± 0.03 to 0.77 ± 0.05 for treatment times of 0, 2, 3 and 5 min, respectively.

To gain insights into the oxidation-induced defect formation process, we used high-resolution core-level C 1s XPS scans to quantify the relative concentrations of graphitic carbon (GC) and defect-like carbon (DC). The C 1s spectra were deconvoluted into C=C (graphitic carbon), C−C (alkylinic carbon), C−O (epoxy), and C=O (carbonyl); C=C is characteristic of GC, whereas C−C, C−O, and C=O are characteristic of DC.[26, 79] Representative deconvoluted spectra for uECNF and ECNF-M3 are shown in **Figure 1d** and **Figure 1e,** respectively. The C 1s spectra for the other two materials are shown in **SI Figure S4**. For details on spectrum deconvolution, see **SI Methods**. **Table 2** summarizes the area percentage of each component ($A_{C=C}$, A_{C-C}, A_{C-O} and $A_{C=O}$) for ECNFs with different oxidation degrees. $A_{C=C}$ decreased after the treatment, indicating that oxidation disrupted sp^2-conjugation. Interestingly, we observe that A_{C-O} and $A_{C=O}$ increased monotonically with treatment time, whereas A_{C-C} did not show such an increasing trend. This observation suggests that whenever a GC was converted into a DC, the DC that formed was an oxygen-containing group. Such a phenomenon may be consistent with an epoxy-driven defect formation mechanism.[8] This mechanism suggests that the break-up of the carbon lattice was triggered by the strain generated from linearly aligned epoxy groups. That is, newly formed DC comprised predominantly oxygen-containing bonds. Increases in both A_{C-O} and $A_{C=O}$ reflect the generation of new defects because epoxy groups can be easily converted to carbonyl groups in an oxidative environment.[80] With conventional heating for 5 min, we observed negligible changes in the morphology, R_I value and O/C ratio of ECNFs (**SI Figure S5**). Hence microwave irradiation is a particularly efficient technique for converting GC to DC in ECNFs, possibly because of hotspots (i.e.,

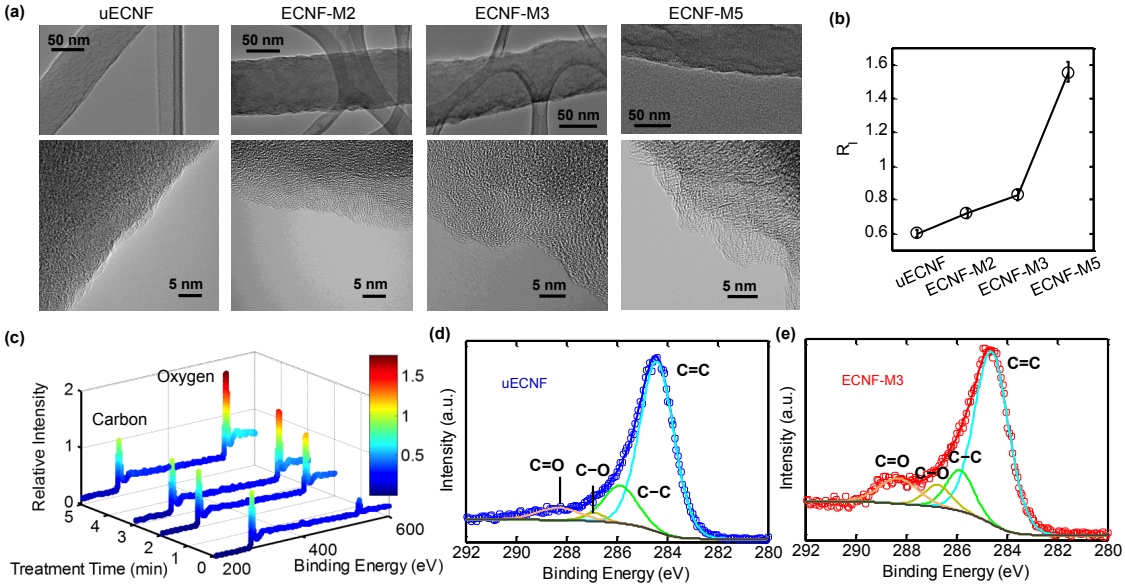

Figure 1. (a) HR-TEM images of uECNF, ECNF-M2, ECNF-M3, and ECNF-M5. The bottom figures show higher-magnification images of the fiber edges. (b) The R_I ratios of uECNF, ECNF-M2, ECNF-M3, and ECNF-M5. (c) Wide-range XPS spectra versus treatment time. The intensity of each spectrum was normalized to that of the carbon peak. (d, e) Deconvolution of the high-resolution core-level C 1s spectrum of (d) uECNF and (e) ECNF-M3.

localized superheating) that arise due to the microwave dielectric heating mechanism.[24] Carbon materials exhibit large dielectric loss factors (tan δ), indicating a high efficiency for converting electromagnetic radiation into heat.[24, 81]

2.2. Electrocapacitive Performance

The forgoing analysis indicates that the microwave-assisted oxidation process provides an effective approach for the manipulation of the structure of ECNFs. Since ECNF material systems[13, 14] and carbon materials with heteroatom chemical moieties[49, 59-62] show great promise for electrocapacitive energy storage applications, we are particularly interested in the relationship between the oxidation-induced structural evolution of ECNFs and their electrochemical properties.

We performed electrochemical characterizations of ECNFs, as-synthesized and microwave-irradiated for different times, in a three-electrode system using a standard aqueous electrolyte (1 M H_2SO_4); the results for uECNF, ECNF-M2, ECNF-M3, and ECNF-M5 are shown in **Figure 2**. Results for other treatment times (1, 2.5, 4, 7, 10, and 15 min) are shown in **SI Figure S6**, which also indicates that the microwave-assisted oxidative treatment is repeatable. Electrochemical evaluation in a three-electrode configuration (where working, counter and reference electrodes are all used) was necessary to locate the redox potentials of surface oxides and to study pseudocapacitive phenomena. The four materials displayed cyclic voltammograms (CVs) of varying shapes and different current densities (**Figure 2a**). It is noteworthy that the difference in gravimetric current density (A/g) among the four materials should not be attributed to their *slightly* different SSAs (**Table 1**), but rather to their different surface chemistries. To verify this, the current was also normalized to the total surface area of the sample. The resulting CVs with areal current densities (μA/cm^2) are shown in **Figure 2b**, which resembles **Figure 2a** in terms of the relative magnitudes of currents across the four different mateirals. The following discussion on CVs is based on **Figure 2b** since the areal current density reflects faithfully the surface chemistries and intrinsic electronic properties of carbon electrode materials.[82, 83] uECNF exhibited a quasi-rectangular CV, indicating a pronounced DL capacitive behavior with minor pseudocapacitive contribution. In contrast, the CV of ECNF-M2 deviated significantly from a rectangular shape. The difference between the anodic and cathodic currents for ECNF-M2 was larger than that for uECNF, especially between 0.2 and 0.6 V, a potential range over which the faradaic reactions of surface oxides occur.[84] This observation indicates that ECNF-M2 showed a marked pseudocapacitive behavior. With an increased degree of

Table 1. Specific surface area (SSA), total pore volume (V_{total}), micropore volume (V_{micro}), and mesopore volume (V_{meso}) for uECNF, ECNF-M2, ECNF-M3, and ECNF-M5. The percentages in the brackets indicate the volume fractions of micropores and mesopores.

Sample	*SSA* ($m^2\,g^{-1}$)	V_{total} ($cm^3\,g^{-1}$)	V_{micro} ($cm^3\,g^{-1}$)	V_{meso} ($cm^3\,g^{-1}$)
uENCF	578	0.326	0.269 (83%)	0.057 (17%)
ENCF-M2	656	0.510	0.395 (77%)	0.115 (23%)
ENCF-M3	670	0.534	0.397 (74%)	0.137 (26%)
ENCF-M5	682	0.592	0.436 (74%)	0.156 (26%)

Table 2. Area percentages (%) of C=C, C−C, C−O and C=O for uECNF, ECNF-M2, ECNF-M3, and ECNF-M5.

Sample	$A_{C=C}$	A_{C-C}	A_{C-O}	$A_{C=O}$
uENCF	74.29	17.34	1.61	6.76
ENCF-M2	68.92	15.45	5.48	10.14
ENCF-M3	68.61	12.95	6.90	11.54
ENCF-M5	54.22	16.25	10.25	19.28

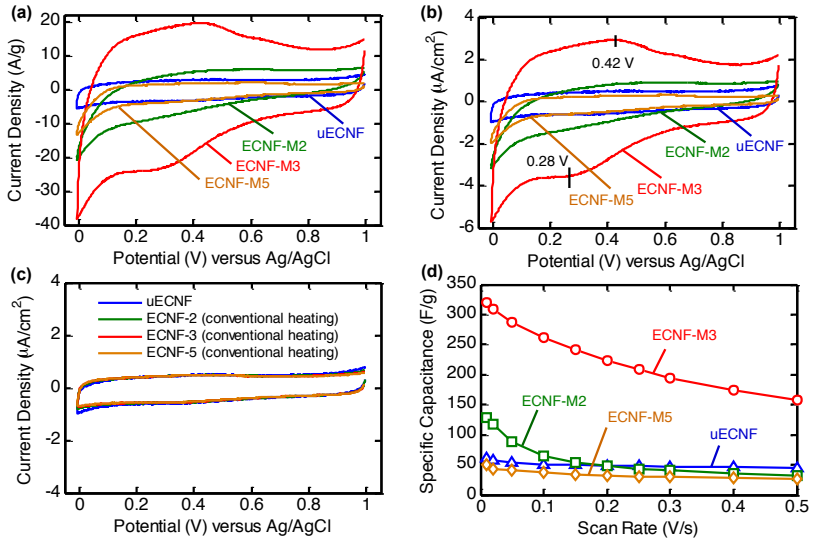

Figure 2. Electrochemical characterization in a three-electrode configuration. (a) CVs of uECNF, ECNF-M2, ECNF-M3, and ECNF-M5 at 0.05 V/s. (b) The same CVs as shown in (a) with currents normalized to the total surface areas. (c) CVs of control samples treated using the conventional heating method (ECNF-2, ECNF-3, and ECNF-5 are samples treated by 2, 3, and 5 min, respective), overlaid with the CV of uECNF. The scan rate is 0.05 V/s. (d) Specific capacitance versus scan rate for uECNF, ECNF-M2, ECNF-M3, and ECNF-M5.

oxidation, ECNF-M3 sustained a higher current density than did uECNF or ECNF-M2. The CV of ECNF-M3 displayed two broad peaks centered at 0.42 and 0.3 V, consistent with the redox reaction between the carbonyl and epoxy groups in an acidic electrolyte solution.[84] Surprisingly, despite its highest O/C ratio, ECNF-M5 exhibited the lowest current density, presumably because over-oxidation caused serious disruption of sp^2-conjugation and loss of structural integrity. The CVs of ECNFs treated by conventional heating were nearly the same as the CV of uECNF (**Figure 2c**); short oxidation treatment without microwave irradiation did not affect the capacitive performance of ECNFs.

Figure 2d shows the specific capacitance of the four material systems as a function of scan rate, calculated from CV measurements (see **SI Methods** for calculation details). The corresponding areal capacitances are shown in **SI Figure S7**. Both the gravimetric and areal capacitances exhibited consistent scan rate dependences. At low scan rates (< 0.1 V/s), ECNF-M2 showed higher capacitances than did uENCF; however, the capacitance of ECNF-M2 decayed with increasing scan rates, and became lower than that of uECNF when the scan rate exceeded 0.1 V/s. The observed overall capacitance had two contributions: pseudocapacitance and DL capacitance. Charging of the pseudocapacitance is a kinetically slow process whereas charging of the DL capacitance is relatively fast.[12] We hypothesize that a higher ECNF oxidation degree might have resulted in a lower DL capacitance; disruption of C=C structures reduces the number of π electrons, leading to a lower density of electronic states (DOS) near the Fermi level (E_F) and thus a lower DL capacitance.[82, 85, 86] At low scan rates, pseudocapacitance dominated and ECNF-M2 showed a higher overall capacitance, while at high scan rates, the DL capacitance dominated and uECNF showed higher overall capacitance.

ECNF-M3 exhibited a higher capacitance than did ECNF-M2 over the entire scan rate range. This is because: (i) compared to ECNF-M2, ECNF-M3 had a higher O/C ratio and thus a higher pseudocapacitance; (ii) $A_{C=C}$ for ECNF-M3 was only slightly lower than that for ECNF-M2, and thus both exhibited similar DL capacitances. The capacitance of ECNF-M3 decayed with increasing scan rate, indicating that the pseudocapacitance with sluggish charging kinetics was the major contribution to the overall capacitance. Generally, the capacitances of ECNF-M2, ECNF-M3, and ECNF-M5 decayed more significantly with an increasing scan rate than did the capacitance of uECNF; for instance, when the scan rate increased from 0.1 to 0.5 V/s, the percentage decay of capacitance for uECNF, ECNF-M2, ECNF-M3, and ECNF-M5 was 10.5%, 49.6%, 40.3% and 30.3%, respectively.

The capacitance of ECNF-M5 was the lowest of all samples tested. A lower $A_{C=C}$ of ECNF-M5 than that of ECNF-M2 or ECNF-M3 indicated a lower DL capacitance. However, unexpectedly, even at a scan rate as low as 0.01 V/s where the pseudocapacitive mechanism dominated, ECNF-M5 exhibited a lower capacitance than did uECNF. We hypothesize that over-oxidation may have led to an inability of ECNF-M5 to support redox reactions of surface oxides due to serious disruption of the graphite structure; it has been reported that oxidation of graphite materials hampers their ability to transfer electrons to initiate surface redox reactions.[87] Additionally, we found that for carbon fibers with different diameters, the relationship between the treatment time and the areal capacitance was consistent (see **SI Figure S8** for a detailed discussion).

The performance of capacitive materials should also be assessed in a two-electrode system (where the reference electrode is not used) because full scale, commercial supercapacitors operate under this configuration.[88] We constructed two-electrode symmetrical supercapacitor cells and measured their performance using various electrochemical characterization techniques; the results are displayed in **Figure 3**. **Figure 3a** shows representative CVs at different scan rates of an ECNF-M3 supercapacitor cell. ECNF-M3 exhibited more rectangular voltammetric profiles when tested in a two-electrode configuration than in a three-electrode configuration (**Figure 2a**), as is typical for pseudocapacitive materials.[88] **Figure 3b** shows the specific capacitances of uECNF, ECNF-M2, ECNF-M3, and ECNF-M5 obtained in a two-electrode cell, which are close to those obtained in the three-electrode system (**Figure 2d**). It is known that for carbon materials the capacitance values obtained with the two different electrode configurations are similar,[36] whereas for conducting polymers the results given by the two different electrode systems are usually disparate.[89] A detailed comparison between the two electrode configurations has been given by Stoller and Ruoff.[88] It is worth noting that ECNF-M3 delivered a specific capacitance of 345 F/g at 0.1 V/s, which is significantly higher than the maximum capacitances of previously reported ECNF-based materials (ca. 130 – 246 F/g).[15, 63-75] Furthermore, at such a high scan rate (*i.e.*, 0.1 V/s), the capacitance value of ECNF-M3 compared favorably to those of many other carbon-based supercapacitor materials,

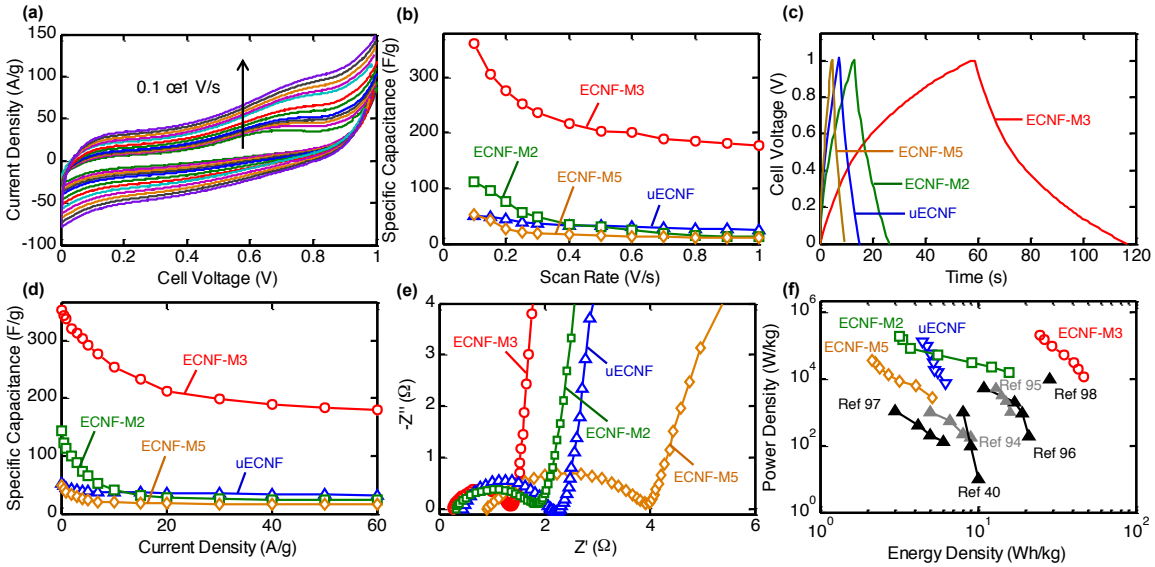

Figure 3. Performance of two-electrode symmetrical supercapacitor cells. (a) Representative CVs of an ECNF-M3 supercapacitor cell at different scan rates from 0.1 to 1 V/s. (b) Specific capacitance as a function of scan rate for uECNF, ECNF-M2, ECNF-M3, and ECNF-M5. (c) Typical galvanostatic charge/discharge profiles at 5 A/g for uECNF, ECNF-M2, ECNF-M3, and ECNF-M5. (d) Specific capacitance versus current density for uECNF, ECNF-M2, ECNF-M3, and ECNF-M5. (e) EIS spectra for uECNF, ECNF-M2, ECNF-M3, and ECNF-M5. (f) Power density versus energy density (Ragone plots) for uECNF, ECNF-M2, ECNF-M3, and ECNF-M5, together with several previously reported high-performance carbon-based capacitive materials. All values are shown on an active mass normalized basis.

including conventional systems such as mesoporous carbon (*ca*. 150 F/g)[37-39] and activated carbon (<120 F/g),[40-42] as well as recently reported carbon nanomaterials such as carbon nanocages (185 F/g),[36] carbon nanococoons (175 F/g),[43] and graphene (ca. 150 – 200 F/g).[44-47]

The capacitive performance of the ECNFs was examined further by chronopotentiometry. Representative galvanostatic charge/discharge profiles at 5 A/g for uECNF, ECNF-M2, ECNF-M3, and ECNF-M5 are shown in **Figure 3c**. All profiles were recorded after 10 CV cycles at 0.1 V/s. The operation voltage was adjusted such that in this potential range the galvanostatic curve exhibited a quasi-triangular form;[36, 37] the optimized operation cell voltage was 1 V for all samples. Among the four samples, ECNF-M3 exhibited the longest charge/discharge time, indicating the highest capacitance. The galvanostatic profile of ECNF-M3 showed a clear deviation from the perfect triangular shape, consistent with a pseudocapacitive contribution from the redox reaction of oxygen-containing surface functionalities. No obvious ohmic drop was observed for ECNF-M3 even at a high current density of 5 A/g, suggesting excellent capacitor performance during the rapid charging-discharging process.[36, 90] **Figure 3d** shows the specific capacitances of uECNF, ECNF-M2, ECNF-M3, and ECNF-M5 at varying current densities, calculated from the chronopotentiometry measurements (see **SI Methods**). At current densities lower than 10 A/g, the capacitance increased in the order ECNF-M5 < uECNF < ECNF-M2 < ECNF-M3, whereas at current densities higher than 10 A/g, the order between uECNF and ECNF-M2 was reversed. Such observations were consistent with the CV measurements with varying scan rates (**Figure 2d and Figure 3b**). Importantly, ECNF-M3 demonstrated high capacitances at the high charge/discharge rates (≥1 A/g),[36] such as 338, 292, 254, 212, and 183 F/g at 1, 5, 10, 20 and 50 A/g, respectively. This rapid charge/discharge capability was similar to that of up-to-date graphene materials;[6, 44-47] such high rate performance is crucial for applications requiring peak power output.[35]

The electrochemical impedance spectrum (EIS) for each of the four materials (**Figure 3e**) consisted of a semicircle in the high frequency range, representing the impedance due to the charge transfer process at the electrode-electrolyte interface, and a nearly vertical line in the low frequency range, indicating a pronounced capacitor behavior.[44, 91] In EIS, the diameter of the semicircle and the intercept on the Z' axis approximate the values of the interfacial charge transfer resistance (R_{ct}) and the solution resistance (R_s), respectively.[22, 44, 91] An equivalent circuit (**Figure S9**) was employed to fit the impedance data and to extract the R_{ct} and R_s values, which reflect the effects of both ion and electron transport. With the oxidation degree increased to an intermediate level, ECNFs exhibited a decrease in both resistances: for uECNF, ECNF-M2 and ECNF-M3, R_s-values were 0.43, 0.32, and 0.25 Ω, respectively, with corresponding R_{ct}-values of 0.81, 1.52, and 1.11 Ω. This trend may have been due to an enhanced mesoporosity and a larger density of oxygen-containing hydrophilic groups. Both factors could facilitate the interaction of the carbon surface with aqueous electrolytes, and thus reduce ionic resistances.[69, 92] On the other hand, despite its large O/C ratio and high mesopore fraction, ECNF-M5 showed the largest resistances (R_s = 0.92 Ω and R_{ct} = 3.07 Ω) among the four systems, which might be attributed to its seriously compromised electron transport properties due to over-oxidation.

Figure 3f shows the Ragone plots (i.e., power density versus energy density) for symmetrical supercapacitor cells constructed with uECNF, ECNF-M2, ECNF-M3, and ECNF-M5. All four systems possessed power densities ranging from 10^3 to 10^6 Wh/kg, which are similar to those of conventional electrolytic capacitors (**SI Figure S10**).[58, 93] Compared to uECNF, ECNF-M2 showed higher energy densities at low power densities and lower energy densities at high power densities. ECNF-M5 showed the worst energy-power

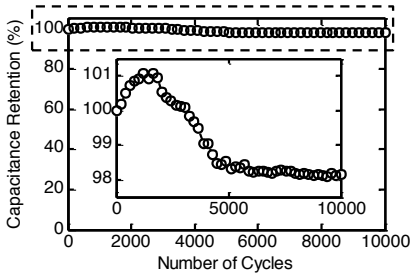

Figure 4. Cycling performance (capacitance retention percentage versus the number of cycles) of an ECNF-M3 supercapacitor cell tested at a current density of 5 A/g. The inset is an enlargement of the dotted rectangle.

combination among the four samples. Remarkably, ECNF-M3 exhibited very high energy densities (from 24.8 to 46.9 Wh/kg) over the entire power density range. This performance is already comparable to that of batteries (**SI Figure S10**).[58, 93] ECNF-M3 demonstrated an energy-power combination comparable to or even better than previously reported high performance carbon-based symmetrical supercapacitor cells (solid triangles in black or gray in **Figure 3f**);[40, 94-98] all values are shown on an active mass normalized basis.

In addition, we examined the electrochemical stability of ECNF-M3 by performing 10000 galvanostatic charge/discharge cycles at a current density of 5 A/g. **Figure 4** shows that its capacitance decayed by only 2 % after 10000 cycles, most of the decay occurring in the first 5000 cycles. That is, ECNF-M3 exhibited excellent cycling performance, a crucial property for practical energy storage applications. Under the same experimental conditions, the capacitances of uECNF, ECNF-M2 and ECNF-M5 decayed by 1%, 1.4%, and 3%, respectively, after 10000 cycles (**SI Figure S11**).

2.3. Electronic and Crystalline Properties

When examining the effect of oxidation degree on the electrocapactive performance of ECNFs, we drew two major conclusions: (i) a higher oxidation degree resulted in a lower DL capacitance; and (ii) over-oxidation disrupted the structural integrity of ECNFs and resulted in their inability to support the pseudocapacitive reactions. To test the first hypothesis, we employed ultraviolet photoelectron spectroscopy (UPS) to probe the electronic structures of ECNFs with different degrees of oxidation. Important information on the DL capacitances of electrode materials can be inferred from their electronic structures.[82, 85, 86] **Figure 5a** shows the measured UPS spectra normalized by the total integrated intensity. E_F is the Fermi level, which sets the zero for binding energy. All four materials exhibited graphite-like valence band structures: the intensities from 0 – 3, 3 – 12, and > 12 eV arise from $p\pi$, $p\sigma$, and $s\sigma$ states, respectively.[95] When the oxidation degree increased, we observed an increase in the high binding energy cutoff (E_{HBC}) (**Figure 5b**), which further indicated a decrease in the work function ($\Phi = E_{photon} - E_{HBC}$,[32, 82] where E_{photon} is the incident photon energy). For graphitic materials, a lower Φ has been found to be associated with a lower DL capacitance.[82, 99] The detailed UPS spectra near E_F (**Figure 5c**) show that the density of π electronic states (0 – 3 eV)[100] decreased in the order: uECNF > ECNF-M2 ≈ ECNF-M3 > ECNF-M5, consistent with the observed decrease in $A_{C=C}$ (**Table 2**). Density functional theory (DFT) calculations also suggest that oxidation of graphitic materials leads to suppression of DOS near E_F.[10, 11] Additionally, the DL capacitance (C_{DL}) of a graphitic material is directly related to the DOS at E_F ($D(E_F)$) according to the Gerischer model:[85, 86, 101]

$$\frac{1}{C_{DL}} = \frac{1}{C_H} + \frac{1}{\sqrt{\varepsilon\varepsilon_0 D(E_F) e_0}} \quad (1)$$

where C_H is the Helmholtz capacitance, which is a constant for a given electrolyte,[86] ε is the dielectric constant, ε_0 is the vacuum permittivity, and e_0 is the electronic charge. The second term on the right hand side of Equation 1 is the reciprocal of the spacecharge capacitance (C_{SC}) derived for graphite electrodes.[85, 86] Equation 1 suggests that a higher oxidation degree, which leads to a lower $D(E_F)$, indeed implies a lower C_{DL}. However, it should be noted that Equation 1 was derived for graphite electrodes without heteroatom chemical moieties. For our ECNFs functionalized with oxygen-containing groups, we must consider another important factor, which is the mismatch in the Fermi levels between the electrode surface and the surface oxides. This mismatch may give rise to a difference in electron energy across the space-charge region ($\Delta\phi_{SC}$) in the electrode phase that could affect the value of C_{SC}.[102]

To delineate the effects of this energy-level mismatch, we investigated the detailed band structures of the ECNF systems. **Figure 5d** depicts the positions of E_F, the valence band (E_V), and the conduction band (E_C) using the vacuum scale for the four samples with different oxidation levels. Because the valence band onset for uECNF was quite close to the Fermi level (**Figure 5c**) possibly due to its semi-metallic nature, we placed the E_V ~0.1 eV below the Fermi level. In contrast, the $D(E_F)$ for ECNF-M2, ECNF-M3, and ECNF-M5 was suppressed due to oxidation,[10, 11] and therefore as an approximation we set their E_V onsets roughly 0.8 eV below E_F, based upon the detailed shapes of their UPS spectra (**Figure 5c**). Molecular modeling within the local DFT of both graphite oxide[10] and oxygen-adsorbed graphene[11] predicts an increase of the finite energy gap at E_F with a higher O/C ratio. Hence we expect that ECNFs with a higher oxidation degree should exhibit a larger ($E_C - E_V$) value; the conduction bands were placed accordingly. **Figure 5d** also displays the energy levels of the dominant redox couple on ECNFs (i.e., carbonyl/epoxy).[84] The energy distribution functions of the occupied and unoccupied states (D_{red} and D_{ox}) are given by Equations 2 and 3, respectively.[103, 104]

$$D_{red} = \frac{1}{\sqrt{4\pi k_B T\lambda}} \exp\left(-\frac{\left(E - E_{F,redox} + \lambda\right)^2}{4k_B T\lambda}\right) \quad (2)$$

$$D_{ox} = \frac{1}{\sqrt{4\pi k_B T\lambda}} \exp\left(-\frac{\left(E - E_{F,redox} - \lambda\right)^2}{4k_B T\lambda}\right) \quad (3)$$

T is the absolute temperature and k_B is the Boltzmann constant. λ is the solvent reorganization energy, which lies in between 0.5 and 1 eV.[103] Here we use a value of 0.5 eV; values between 0.5 and 1 eV do not affect the following discussions and conclusions. The Fermi level of the redox couple, $E_{F,redox}$, was determined from its formal potential of 0.35 V versus Ag/AgCl.[84, 104] As manifested in **Figure 5d**, $E_{F,redox}$ was different from the Fermi levels of the four ECNF systems at the electrode surface. At equilibrium, the Fermi levels of the *bulk* electrode and the surface redox couple must match, which

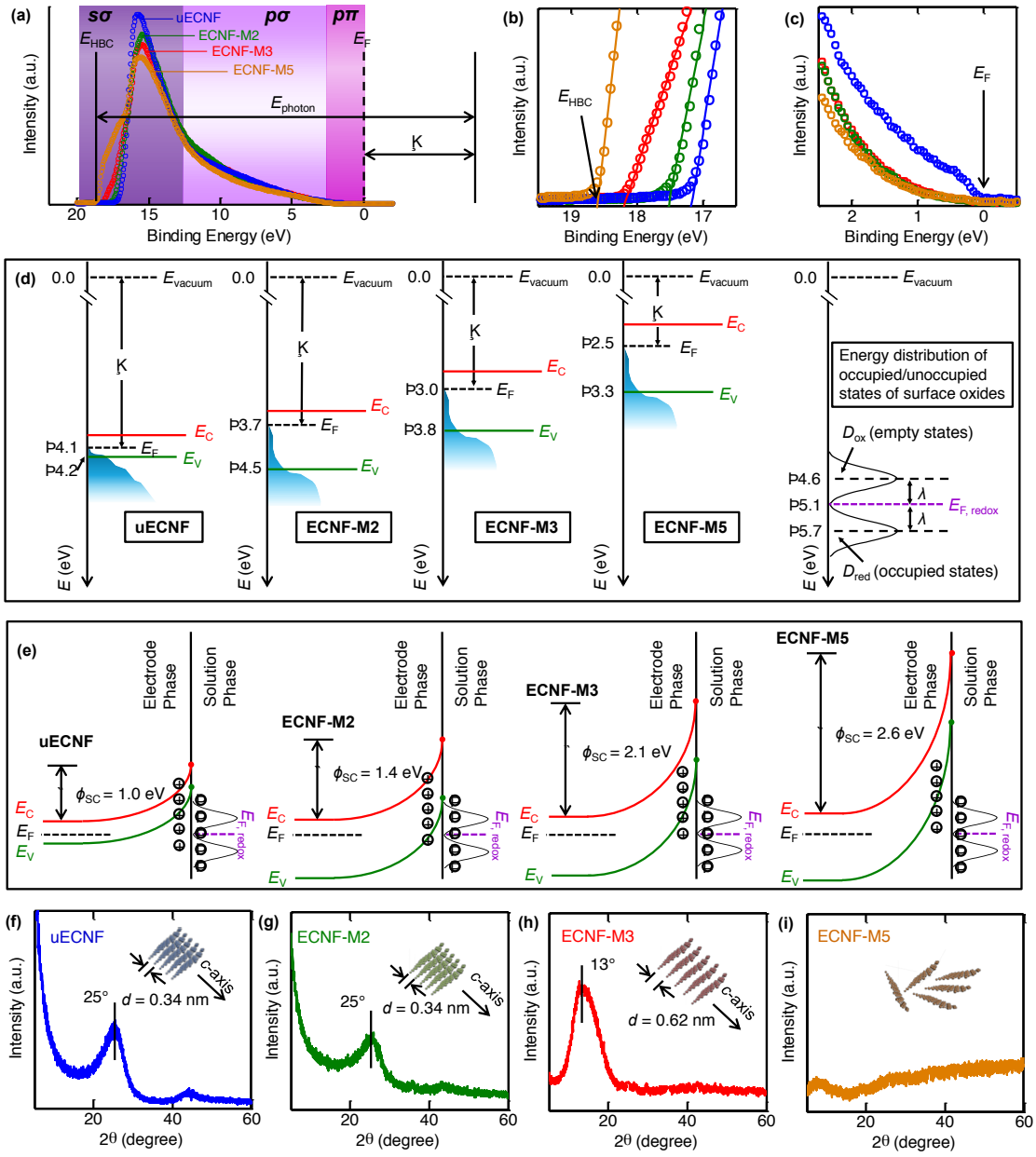

Figure 5. (a) Full UPS spectra of uECNF, ECNF-M2, ECNF-M3, and ECNF-M5. Gold was used as the internal standard to locate the Fermi level. (b) Detailed UPS spectra at the high binding energy regime. (c) Detailed UPS spectra near the Fermi level. (d) Band structures of uECNF, ECNF-M2, ECNF-M3, and ECNF-M5, together with the energy distribution of the occupied and unoccupied states of the surface oxide. (e) Schematic illustration of the band bending effect. (f-i) XRD patterns of (f) uECNF, (g) ECNF-M2, (h) ECNF-M3, and (i) ECNF-M5

causes band bending, as illustrated in **Figure 5e**. How this band bending occurs can be understood by the following arguments. The E_V levels of the ECNF samples were higher than the unoccupied D_{ox} level of the surface oxide, which displayed electron-acceptor characteristics, consistent with literature reports.[59, 105] Therefore, electrons would have transferred from the electrode to the surface oxide; the electrode phase then became positively charged. The excess positive charge did not reside at the surface, but instead was distributed in the space-charge region. The resulting electric field in the space-charge region affected the local energy of the electrons. The positive charge in the space-charge region caused the band energies to become more negative with increasing distance into the electrode; then the bands remained flat in the field-free bulk. **Figure 5e** shows clearly that ECNFs with different oxidation degrees exhibited significantly different $\Delta\phi_{SC}$. Hence for the ECNF systems, the C_{SC} term should be re-evaluated using the Mott-Schottky equation that takes $\Delta\phi_{SC}$ into account:[106]

$$\frac{1}{C_{SC}} = \sqrt{\frac{2}{\varepsilon\varepsilon_0 N}\left(\Delta\phi_{SC} - \frac{k_B T}{e_0}\right)} \tag{4}$$

where N is the charge carrier concentration. N is proportionally related to $D(E_F)$ through Equation 5, where the integral has the value of 0.693 $k_B T$.[107]

$$N = D(E_F) \times 2\int_0^{\infty} \left(1 + \exp\left(E/k_B T\right)\right)^{-1} dE \tag{5}$$

For uECNF, ECNF-M2, ECNF-M3 and ECNF-M5, the $\Delta\phi_{SC}$ value increased from 1.0 to 1.4 to 2.1 to 2.6 eV. Also, given the proportionality between N and $D(E_F)$, a higher oxidation degree implies a lower value for N. From Equation 4, it can be seen that both an increase in $\Delta\phi_{SC}$ and a decrease in N result in a lower C_{SC}. Therefore, after considering the effect of $\Delta\phi_{SC}$, our earlier conclusion that a higher oxidation degree resulted in a lower double-layer capacitance is substantiated.

From the discussion above, we see that the electronic structures of the four ECNF systems were significantly different. Thus we next attempt to examine if such differences could have affected the redox reactions of the surface oxide, which govern the redox-based pseudocapacitance.[35, 108] A question of particular interest is whether a much lower pseudocapacitance for ECNF-M5 than for ECNF-M3 could be explained by the difference in electronic structure between them. Several previous studies,[109, 110] essentially based on the work of Marcus[111] and Hush,[112] suggest that the electron transfer rate (k_{ET}) of a redox species depends strongly on the $D(E_F)$ of the electrode material. Although different electron transfer models have been proposed, the general consensus is that a lower $D(E_F)$ leads to a lower k_{ET}. Our observed decreasing trend of $D(E_F)$ with a higher oxidation level suggests that k_{ET} may have decreased from uECNF to ECNF-M2 to ECNF-M3 to ECNF-M5. Some recent works also show that in addition to $D(E_F)$, other factors can affect k_{ET}, such as the distribution of DOS[103] and the electrochemical potential applied to the electrode.[113] However, during CV measurements, k_{ET} influences only the shape of the voltammogram, but not its integrated area, which is proportional only to the density of the surface oxide at slow scan rates.[102] Hence the pseudocapacitance (i.e., the integrated area of the CV divided by the voltage window) should not be affected by k_{ET}. Therefore, the observation that ECNF-M5 had the highest O/C ratio but showed the lowest capacitance cannot be explained by its possibly very low k_{ET}. Additionally, a given redox reaction can display remarkably different degrees of reversibility when electrodes with varying band structures are employed.[104, 114, 115] Thus another possible explanation is that the surface oxide may have shown an irreversible behavior on ECNF-M5, which led to a low pseudocapacitance. If this were true, the initial CV profile (i.e., the first scan) of ECNF-M5 should show comparable or even higher current densities than those of ECNF-M3, and the current densities should decrease with an increasing number of CV cycles (a sign of reaction irreversibility). However, we performed multiple CV scans using ECNF-M5 and observed no significant changes between different cycles; also, the first CV scan already exhibited very low current densities and showed no redox peaks (**SI Figure S12**). A more plausible explanation is our second hypothesis: ECNF-M5 lost microstructural integrity due to over-oxidation and thus could not initiate the redox reaction of the surface oxide.

To examine this hypothesis, we used X-ray diffraction (XRD) to probe the structural order of ECNFs with different degrees of oxidation (**Figure 5f-i**). uECNF displayed a diffraction peak at 2θ = 25°, indicating good layer regularity with an interlayer spacing (d) of 0.34 nm along the c-axis according to the Bragg equation. ECNF-M2 exhibited a diffraction pattern similar to that of uECNF, suggesting that the ordered crystalline structure was preserved after the 2 min treatment.

ECNF-M3 showed a diffraction peak at a lower 2θ angle of 13°, suggesting a larger d spacing of 0.62 nm, due to the oxidation-induced expansion of the graphite structure.[116] Also, the appearance of this diffraction peak indicates that ECNF-M3 maintained a long-range ordered crystalline structure. Moreover, the expanded interlayer distance was conducive to accommodating the electrolyte ion for enhancing the capacitance.[117] This may have been another contributing factor for the performance disparity between ECNF-M3 and ECNF-M2. Both materials had close DL capacitances, indicated by their similar $D(E_F)$ and $A_{C=C}$, but their capacitance ratio (~2.5) was larger than the ratio of the O/C values between them (1.3). Hence, a higher O/C ratio alone may not suffice to explain the higher capacitance observed for ENCF-M3. The better ion accommodation capacity of ECNF-M3 may also have contributed to its better capacitive performance.

In contrast to the other three material systems, ECNF-M5 displayed no XRD diffraction peaks, indicating a complete loss of ordered crystalline structure (*i.e.*, exfoliation). The lack of stacking order between graphene sheets would have made it difficult for the material to transfer electrons efficiently to support the surface redox reactions; thus ECNF-M5 could not exhibit pseudocapacitive behavior. This conclusion is consistent with the observation that, in the potential range 0.2 – 0.6 V where the redox reactions of surface oxides occur, ECNF-M5 showed an even lower current density than did uECNF (**Figure 2b**). Note that even though the difference in the capacitances between ECNF-M5 and uECNF was subtle, the two samples behaved quite differently. The scan rate-dependent CV profiles (**SI Figure S13**) show that ECNF-M5 displayed a strong resistive behavior with greatly distorted CV shapes, while uECNF displayed a DL capacitive behavior with well-maintained quasi-rectangular CV shapes even at high scan rates. For oxidation of graphite, a complete loss of order in the c-direction has rarely been observed. The easy loss of structural integrity observed here may be specific to a turbostratic ECNF with rotationally disordered layers along the c-axis. The interlayer interaction in ECNFs may be weaker than that in graphite with a well-defined AB hexagonal stacking structure. Additionally, ECNFs contain only ~4 graphene layers in the c-direction (crystallite size L_c is ~1 nm),[21] whereas graphite typically contains ~61 layers (L_c is ~20 nm).[87] It may be easier to dissemble the crystalline domains with fewer stacking layers. Moreover, microwave irradiation increases the mobility of the intercalating agent during oxidation (i.e., SO_4^{2-}),[26] and may contribute to the structure disruption.

A plausible criterion for over-oxidation of ECNFs may be inferred from previous studies on the detailed structures of oxidized graphite. Graphite with a saturated oxidation degree consists of laminar carbon networks that adopt a wrinkled hexagonal structure with a typical interlayer spacing of 0.6 to 0.7 nm.[10, 118-120] Such a graphite structure has a coverage of the carbon network of approximately 50% oxygen (i.e., O/C ratio ≈ 0.5).[10, 118, 121, 122] Insertion of more oxygen atoms into the carbon network should cause the breaking of the crystalline structure and significant changes in the electronic properties; over-oxidized graphite may exhibit an insulator-like behavior.[10, 118-122] ECNF-M3 had an O/C ratio of 0.56 and an interlayer distance of 0.62 nm (determined from XRD), whereas ECNF-M5 had an O/C ratio of 0.77 and a disrupted crystalline structure. These results suggest that over-oxidation of

ECNFs may occur when the oxidative treatment gives rise to an O/C ratio > ~0.5.

It would be useful to be able to predict the oxidation level of ECNFs quantitatively in terms of the treatment time. A possible method is the development of a kinetic model on oxidation of ECNFs, which allows calculation of the concentration of oxygen-containing groups as a function of time. However, we were currently unable to establish a quantitative relationship between the oxidation level and the treatment time for the following reasons. First, it has been widely recognized that it is difficult to measure the actual temperature on the "hotspots" (particularly for heterogeneous reactions) associated with localized superheating due to the microwave dielectric heating mechanism.[24] The local temperature should influence the oxidation kinetics significantly. Second, it is challenging to identify the rate-limiting step due to generally complicated oxidation mechanisms, and to determine the activation energy accurately, which requires detailed molecular-level simulation on the oxidation process of a specific carbon system.[7, 8, 26]

3. Conclusion

We have demonstrated controlled structure variation of PAN-derived turbostratic ECNFs using a microwave-assisted oxidation process, and have elucidated the relationships between the oxidation degree of the ECNFs and their structural, electronic, and electrochemical properties. Precise control over the oxidation level of turbostratic carbon materials is indispensable for varying their energy storage capabilities. We found that ECNFs with an intermediate oxidation degree exhibited ultrahigh capacitances at high scan rates or current densities, an excellent energy-power combination, and good cycling performance. We have identified three important factors required to achieve optimal capacitive performance: (i) abundant surface oxides available for pseudocapactive energy storage; (ii) microstructural integrity for transporting electrons to support the redox reactions of these oxides; and (iii) an appropriate interlayer spacing for enhancing the ability to accommodate ions. Our study provides useful insights into the structure-property relationship of graphitic systems, especially those with abundant edge sites,[30-34] and suggests an inexpensive, controllable, and highly efficient means for manipulating carbon materials. The ECNF material with controlled DOS, work function and band structure may be useful in other technological areas where the carbon electronic properties govern the performance, and thus can be used for the development of a variety of electrochemical, electronic, and optical devices, such as electrochemical biosensors, fuel cells, metal-air batteries, field-effect transistors, and photo-electrochemical cells.

Supporting Information

Experimental details, and supplementary tables and figures. This material is available free of charge via the Internet at http://pubs.acs.org.

References

[1] R. L. McCreery, *Chem Rev* **2008**, *108*, 2646.

[2] Y. P. Zhai, Y. Q. Dou, D. Y. Zhao, P. F. Fulvio, R. T. Mayes, S. Dai, *Adv Mater* **2011**, *23*, 4828.

[3] X. Mao, G. C. Rutledge, T. A. Hatton, *Nano Today* **2014**, *9*, 405.

[4] K. P. Gong, F. Du, Z. H. Xia, M. Durstock, L. M. Dai, *Science* **2009**, *323*, 760.

[5] D. Y. Pan, S. Wang, B. Zhao, M. H. Wu, H. J. Zhang, Y. Wang, et al., *Chem Mater* **2009**, *21*, 3136.

[6] Y. W. Zhu, S. Murali, M. D. Stoller, K. J. Ganesh, W. W. Cai, P. J. Ferreira, et al., *Science* **2011**, *332*, 1537.

[7] P. M. Ajayan, B. I. Yakobson, *Nature* **2006**, *441*, 818.

[8] J. L. Li, K. N. Kudin, M. J. McAllister, R. K. Prud'homme, I. A. Aksay, R. Car, *Phys Rev Lett* **2006**, *96*.

[9] D. V. Kosynkin, A. L. Higginbotham, A. Sinitskii, J. R. Lomeda, A. Dimiev, B. K. Price, et al., *Nature* **2009**, *458*, 872.

[10] R. J. W. E. Lahaye, H. K. Jeong, C. Y. Park, Y. H. Lee, *Phys Rev B* **2009**, *79*.

[11] J. Ito, J. Nakamura, A. Natori, *J Appl Phys* **2008**, *103*.

[12] E. Frackowiak, F. Beguin, *Carbon* **2001**, *39*, 937.

[13] M. Inagaki, Y. Yang, F. Y. Kang, *Adv Mater* **2012**, *24*, 2547.

[14] X. W. Mao, T. A. Hatton, G. C. Rutledge, *Curr Org Chem* **2013**, *17*, 1390.

[15] C. Kim, B. T. N. Ngoc, K. S. Yang, M. Kojima, Y. A. Kim, Y. J. Kim, et al., *Adv Mater* **2007**, *19*, 2341.

[16] J. S. Huang, D. W. Wang, H. Q. Hou, T. Y. You, *Adv Funct Mater* **2008**, *18*, 441.

[17] T. H. Hwang, Y. M. Lee, B. S. Kong, J. S. Seo, J. W. Choi, *Nano Lett* **2012**, *12*, 802.

[18] Y. Yu, L. Gu, C. L. Wang, A. Dhanabalan, P. A. van Aken, J. Maier, *Angew Chem Int Edit* **2009**, *48*, 6485.

[19] Y. Yu, L. Gu, C. B. Zhu, P. A. van Aken, J. Maier, *J Am Chem Soc* **2009**, *131*, 15984.

[20] C. Kim, K. S. Yang, M. Kojima, K. Yoshida, Y. J. Kim, Y. A. Kim, et al., *Adv Funct Mater* **2006**, *16*, 2393.

[21] X. W. Mao, F. Simeon, G. C. Rutledge, T. A. Hatton, *Adv Mater* **2013**, *25*, 1309.

[22] X. W. Mao, X. Q. Yang, G. C. Rutledge, T. A. Hatton, *Acs Appl Mater Inter* **2014**, *6*, 3394.

[23] B. Kumar, M. Asadi, D. Pisasale, S. Sinha-Ray, B. A. Rosen, R. Haasch, et al., *Nat Commun* **2013**, *4*.

[24] C. O. Kappe, *Angew Chem Int Edit* **2004**, *43*, 6250.

[25] A. Centrone, Y. Yang, S. Speakman, L. Bromberg, G. C. Rutledge, T. A. Hatton, *J Am Chem Soc* **2010**, *132*, 15687.

[26] P. L. Chiu, D. D. T. Mastrogiovanni, D. G. Wei, C. Louis, M. Jeong, G. Yu, et al., *J Am Chem Soc* **2012**, *134*, 5850.

[27] J. A. Gerbec, D. Magana, A. Washington, G. F. Strouse, *J Am Chem Soc* **2005**, *127*, 15791.

[28] T. Lv, L. K. Pan, X. J. Liu, T. Lu, G. Zhu, Z. Sun, *J Alloy Compd* **2011**, *509*, 10086.

[29] Y. Liu, D. W. Wang, L. Xu, H. Q. Hou, T. Y. You, *Biosens Bioelectron* **2011**, *26*, 4585.

[30] A. Ambrosi, T. Sasaki, M. Pumera, *Chem-Asian J* **2010**, *5*, 266.

[31] A. Ambrosi, M. Pumera, *Chem-Eur J* **2010**, *16*, 10946.

[32] E. C. Landis, K. L. Klein, A. Liao, E. Pop, D. K. Hensley, A. V. Melechko, et al., *Chem Mater* **2010**, *22*, 2357.

[33] X. L. Li, H. L. Wang, J. T. Robinson, H. Sanchez, G. Diankov, H. J. Dai, *J Am Chem Soc* **2009**, *131*, 15939.

[34]Y. F. Lu, S. T. Lo, J. C. Lin, W. J. Zhang, J. Y. Lu, F. H. Liu, et al., *Acs Nano* **2013**, *7*, 6522.
[35]P. Simon, Y. Gogotsi, *Nat Mater* **2008**, *7*, 845.
[36]K. Xie, X. T. Qin, X. Z. Wang, Y. N. Wang, H. S. Tao, Q. Wu, et al., *Adv Mater* **2012**, *24*, 347.
[37]B. Liu, H. Shioyama, T. Akita, Q. Xu, *J Am Chem Soc* **2008**, *130*, 5390.
[38]W. R. Li, D. H. Chen, Z. Li, Y. F. Shi, Y. Wan, G. Wang, et al., *Carbon* **2007**, *45*, 1757.
[39]H. J. Liu, W. J. Cui, L. H. Jin, C. X. Wang, Y. Y. Xia, *Journal of Materials Chemistry* **2009**, *19*, 3661.
[40]V. Ruiz, C. Blanco, R. Santamaria, J. M. Ramos-Fernandez, M. Martinez-Escandell, A. Sepulveda-Escribano, et al., *Carbon* **2009**, *47*, 195.
[41]M. S. Balathanigaimani, W. G. Shim, M. J. Lee, C. Kim, J. W. Lee, H. Moon, *Electrochem Commun* **2008**, *10*, 868.
[42]D. Lozano-Castello, D. Cazorla-Amoros, A. Linares-Solano, S. Shiraishi, H. Kurihara, A. Oya, *Carbon* **2003**, *41*, 1765.
[43]J. A. Zhang, K. X. Wang, S. J. Guo, S. P. Wang, Z. Q. Liang, Z. M. Chen, et al., *Acs Appl Mater Inter* **2014**, *6*, 2192.
[44]X. Li, X. B. Zang, Z. Li, X. M. Li, P. X. Li, P. Z. Sun, et al., *Adv Funct Mater* **2013**, *23*, 4862.
[45]X. W. Yang, J. W. Zhu, L. Qiu, D. Li, *Adv Mater* **2011**, *23*, 2833.
[46]X. H. An, T. J. Simmons, R. Shah, C. Wolfe, K. M. Lewis, M. Washington, et al., *Nano Lett* **2010**, *10*, 4295.
[47]M. D. Stoller, S. J. Park, Y. W. Zhu, J. H. An, R. S. Ruoff, *Nano Lett* **2008**, *8*, 3498.
[48]G. P. Wang, L. Zhang, J. J. Zhang, *Chem Soc Rev* **2012**, *41*, 797.
[49]J. Yan, Q. Wang, T. Wei, Z. J. Fan, *Adv Energy Mater* **2014**, *4*.
[50]Z. Y. Cao, B. Q. Wei, *Energ Environ Sci* **2013**, *6*, 3183.
[51]C. Sassoye, C. Laberty, H. Le Khanh, S. Cassaignon, C. Boissiere, M. Antonietti, et al., *Adv Funct Mater* **2009**, *19*, 1922.
[52]Z. S. Wu, D. W. Wang, W. Ren, J. Zhao, G. Zhou, F. Li, et al., *Adv Funct Mater* **2010**, *20*, 3595.
[53]S. Chen, J. W. Zhu, X. D. Wu, Q. F. Han, X. Wang, *Acs Nano* **2010**, *4*, 2822.
[54]Z. S. Wu, W. C. Ren, D. W. Wang, F. Li, B. L. Liu, H. M. Cheng, *Acs Nano* **2010**, *4*, 5835.
[55]Q. Wu, Y. X. Xu, Z. Y. Yao, A. R. Liu, G. Q. Shi, *Acs Nano* **2010**, *4*, 1963.
[56]Z. Q. Niu, P. S. Luan, Q. Shao, H. B. Dong, J. Z. Li, J. Chen, et al., *Energ Environ Sci* **2012**, *5*, 8726.
[57]X. Mao, G. C. Rutledge, T. A. Hatton, *Langmuir : the ACS journal of surfaces and colloids* **2013**, *29*, 9626.
[58]X. Mao, F. Simeon, D. S. Achilleos, G. C. Rutledge, T. A. Hatton, *J Mater Chem A* **2013**, *1*, 13120.
[59]L. Zhao, L. Z. Fan, M. Q. Zhou, H. Guan, S. Y. Qiao, M. Antonietti, et al., *Adv Mater* **2010**, *22*, 5202.
[60]Y. Fang, B. Luo, Y. Y. Jia, X. L. Li, B. Wang, Q. Song, et al., *Adv Mater* **2012**, *24*, 6348.
[61]L. F. Chen, X. D. Zhang, H. W. Liang, M. G. Kong, Q. F. Guan, P. Chen, et al., *Acs Nano* **2012**, *6*, 7092.
[62]Z. S. Wu, A. Winter, L. Chen, Y. Sun, A. Turchanin, X. L. Feng, et al., *Adv Mater* **2012**, *24*, 5130.
[63]C. Kim, K. S. Yang, *Appl Phys Lett* **2003**, *83*, 1216.
[64]C. Kim, S. H. Park, W. J. Lee, K. S. Yang, *Electrochim Acta* **2004**, *50*, 877.
[65]C. Kim, J. S. Kim, S. J. Kim, W. J. Lee, K. S. Yang, *J Electrochem Soc* **2004**, *151*, A769.
[66]C. Kim, K. S. Yang, W. J. Lee, *Electrochem Solid St* **2004**, *7*, A397.
[67]C. Kim, Y. O. Choi, W. J. Lee, K. S. Yang, *Electrochim Acta* **2004**, *50*, 883.
[68]C. Kim, *J Power Sources* **2005**, *142*, 382.
[69]Y. W. Ju, S. H. Park, H. R. Jung, W. J. Lee, *J Electrochem Soc* **2009**, *156*, A489.
[70]H. T. Niu, J. Zhang, Z. L. Xie, X. G. Wang, T. Lin, *Carbon* **2011**, *49*, 2380.
[71]B. H. Kim, K. S. Yang, H. G. Woo, *Electrochem Commun* **2011**, *13*, 1042.
[72]B. H. Kim, K. S. Yang, Y. A. Kim, Y. J. Kim, B. An, K. Oshida, *J Power Sources* **2011**, *196*, 10496.
[73]J. S. Im, S. W. Woo, M. J. Jung, Y. S. Lee, *J Colloid Interface Sci* **2008**, *327*, 115.
[74]B. H. Kim, K. S. Yang, H. G. Woo, *J Nanosci Nanotechno* **2011**, *11*, 7193.
[75]S. J. Park, S. H. Im, *B Korean Chem Soc* **2008**, *29*, 777.
[76]X. Mao, T. A. Hatton, *Ind Eng Chem Res* **2015**, *54*, 4033.
[77]X. W. Mao, W. D. Tian, J. Wu, G. C. Rutledge, T. A. Hatton, *J Am Chem Soc* **2015**, *137*, 1348.
[78]M. A. Pimenta, G. Dresselhaus, M. S. Dresselhaus, L. G. Cancado, A. Jorio, R. Saito, *Phys Chem Chem Phys* **2007**, *9*, 1276.
[79]A. Ambrosi, M. Pumera, *Chem-Eur J* **2013**, *19*, 4748.
[80]A. L. Higginbotham, D. V. Kosynkin, A. Sinitskii, Z. Z. Sun, J. M. Tour, *Acs Nano* **2010**, *4*, 2059.
[81]M. Hotta, M. Hayashi, M. T. Lanagan, D. K. Agrawal, K. Nagata, *Isij Int* **2011**, *51*, 1766.
[82]J. D. Wiggins-Camacho, K. J. Stevenson, *J Phys Chem C* **2009**, *113*, 19082.
[83]J. L. Xia, F. Chen, J. H. Li, N. J. Tao, *Nat Nanotechnol* **2009**, *4*, 505.
[84]Y. T. Kim, T. Mitani, *J Power Sources* **2006**, *158*, 1517.
[85]H. Gerischer, R. Mcintyre, D. Scherson, W. Storck, *J Phys Chem-Us* **1987**, *91*, 1930.
[86]H. Gerischer, *J Phys Chem-Us* **1985**, *89*, 4249.
[87]B. R. S. Lemos, I. F. Teixeira, B. F. Machado, M. R. A. Alves, J. P. de Mesquita, R. R. Ribeiro, et al., *J Mater Chem A* **2013**, *1*, 9491.
[88]M. D. Stoller, R. S. Ruoff, *Energ Environ Sci* **2010**, *3*, 1294.
[89]K. V, E. Frackowiak, F. Beguin, *Electrochim Acta* **2005**, *50*, 2499.
[90]K. X. Wang, Y. G. Wang, Y. R. Wang, E. Hosono, H. S. Zhou, *J Phys Chem C* **2009**, *113*, 1093.
[91]L. L. Zhang, X. Zhao, M. D. Stoller, Y. W. Zhu, H. X. Ji, S. Murali, et al., *Nano Lett* **2012**, *12*, 1806.
[92]B. H. Park, J. H. Choi, *Electrochim Acta* **2010**, *55*, 2888.
[93]A. G. Pandolfo, A. F. Hollenkamp, *J Power Sources* **2006**, *157*, 11.
[94]E. Raymundo-Pinero, F. Leroux, F. Beguin, *Adv Mater* **2006**, *18*, 1877.
[95]J. Chmiola, G. Yushin, Y. Gogotsi, C. Portet, P. Simon, P. L. Taberna, *Science* **2006**, *313*, 1760.
[96]H. L. Wang, Z. Li, J. K. Tak, C. M. B. Holt, X. H. Tan, Z. W. Xu, et al., *Carbon* **2013**, *57*, 317.

[97]W. Xing, S. Z. Qiao, R. G. Ding, F. Li, G. Q. Lu, Z. F. Yan, et al., *Carbon* **2006**, *44*, 216.
[98]Y. Wang, Z. Q. Shi, Y. Huang, Y. F. Ma, C. Y. Wang, M. M. Chen, et al., *J Phys Chem C* **2009**, *113*, 13103.
[99]D. Jana, C. L. Sun, L. C. Chen, K. H. Chen, *Prog Mater Sci* **2013**, *58*, 565.
[100] F. R. Mcfeely, Kowalczy.Sp, L. Ley, R. G. Cavell, R. A. Pollak, D. A. Shirley, *Phys Rev B* **1974**, *9*, 5268.
[101] H. V. Patten, K. E. Meadows, L. A. Hutton, J. G. Iacobini, D. Battistel, K. McKelvey, et al., *Angew Chem Int Edit* **2012**, *51*, 7002.
[102] A. J. Bard, L. R. Faulkner, *Electrochemical methods : fundamentals and applications*, 2nd ed., Wiley, New York, **2001**.
[103] R. Sharma, J. H. Baik, C. J. Perera, M. S. Strano, *Nano Lett* **2010**, *10*, 398.
[104] C. G. Zoski, *Handbook of electrochemistry*, 1st ed., Elsevier, Amsterdam ; Boston, **2007**.
[105] U. N. Maiti, W. J. Lee, J. M. Lee, Y. Oh, J. Y. Kim, J. E. Kim, et al., *Adv Mater* **2014**, *26*, 40.
[106] H. Gerischer, R. Mcintyre, *J Chem Phys* **1985**, *83*, 1363.
[107] J. S. Blakemore, *Semiconductor statistics*, Pergamon Press, Oxford, New York,, **1962**.
[108] X. Zhao, B. M. Sanchez, P. J. Dobson, P. S. Grant, *Nanoscale* **2011**, *3*, 839.
[109] W. J. Royea, T. W. Hamann, B. S. Brunschwig, N. S. Lewis, *J Phys Chem B* **2006**, *110*, 19433.
[110] R. J. Forster, P. Loughman, T. E. Keyes, *J Am Chem Soc* **2000**, *122*, 11948.
[111] R. A. Marcus, *J Chem Phys* **1956**, *24*, 966.
[112] N. S. Hush, *J Chem Phys* **1958**, *28*, 962.
[113] R. Nissim, C. Batchelor-McAuley, M. C. Henstridge, R. G. Compton, *Chem Commun* **2012**, *48*, 3294.
[114] P. G. Santangelo, G. M. Miskelly, N. S. Lewis, *J Phys Chem-Us* **1988**, *92*, 6359.
[115] S. N. Frank, A. J. Bard, *J Am Chem Soc* **1975**, *97*, 7427.
[116] T. F. Yeh, J. M. Syu, C. Cheng, T. H. Chang, H. S. Teng, *Adv Funct Mater* **2010**, *20*, 2255.
[117] J. J. Yoo, K. Balakrishnan, J. S. Huang, V. Meunier, B. G. Sumpter, A. Srivastava, et al., *Nano Lett* **2011**, *11*, 1423.
[118] M. Mermoux, Y. Chabre, A. Rousseau, *Carbon* **1991**, *29*, 469.
[119] A. Lerf, H. Y. He, M. Forster, J. Klinowski, *J Phys Chem B* **1998**, *102*, 4477.
[120] T. Szabo, O. Berkesi, P. Forgo, K. Josepovits, Y. Sanakis, D. Petridis, et al., *Chem Mater* **2006**, *18*, 2740.
[121] A. Buchsteiner, A. Lerf, J. Pieper, *J Phys Chem B* **2006**, *110*, 22328.
[122] D. W. Boukhvalov, M. I. Katsnelson, *J Am Chem Soc* **2008**, *130*, 10697.

TOC Figure